Structural control of plasmon resonance in molecularly linked metal oxide nanocrystal gel assemblies

Jiho Kang,[†,§] Zachary M. Sherman,[†,§] Diana L. Conrad,[‡] Hannah S. N. Crory,[‡] Manuel N. Dominguez,[‡] Stephanie A. Valenzuela,[‡] Eric V. Anslyn,[*,‡] Thomas M. Truskett,[*,†,¶] and Delia J. Milliron[*,†,‡]

†*McKetta Department of Chemical Engineering, University of Texas at Austin, 200 E Dean Keeton St, Austin, Texas 78712, United States*

‡*Department of Chemistry, University of Texas at Austin, 2506 Speedway, Austin, Texas 78712, United States*

¶*Department of Physics, University of Texas at Austin, 2515 Speedway, Austin, Texas 78712, United States*

§*These authors contributed equally to this work.*

E-mail: anslyn@austin.utexas.edu; truskett@che.utexas.edu; milliron@che.utexas.edu

Abstract

Nanocrystal gels exhibit collective optical phenomena based on interactions between their constituent building blocks. However, their inherently disordered structures have made it challenging to understand, predict, or design properties like optical absorption spectra that are sensitive to the coupling between the plasmon resonances of the individual nanocrystals. Here, we bring indium tin oxide nanocrystal gels under chemical control and show that their infrared absorption can be predicted and systematically

tuned by selecting the nanocrystal sizes and compositions, and molecular structures of the link-mediating surface ligands. Thermoreversible assemblies with metal-terpyridine links form reproducible gel architectures, enabling us to derive a plasmon ruler that governs the spectral shifts upon gelation predicated on the nanocrystal and ligand compositions. This empirical guide is validated using large-scale, many-bodied simulations to compute the optical spectra of gels with varied structural parameters. Based on the derived plasmon ruler, we design and demonstrate a nanocrystal mixture whose spectrum exhibits distinctive line narrowing upon assembly.

Key words: colloidal gel, localized surface plasmon resonance, mutual polarization, plasmon coupling, dynamic covalent bonding, plasmon ruler.

Nanoparticles with a high density of free electrons, including noble metals like gold and silver and degenerately doped colloidal metal oxides such as tin-doped indium oxide ($Sn:In_2O_3$, or ITO) nanocrystals, display strong light-matter interactions due to localized surface plasmon resonance (LSPR). In ITO nanocrystals, the resonance is widely tunable through synthetic control of the size, shape, and aliovalent doping of the inorganic core.[1–6] While deriving properties from the individual particles, nanoparticle assemblies also manifest structure-dependent collective behavior, such as LSPR coupling, motivating extensive research on the optical response of nanodimers, small clusters, and extended structures.[7–11] In periodic superlattices assembled from plasmonic nanoparticles, tuning of the optical properties has been demonstrated by varying the length of DNA links or the molecular weight of surface-grafted molecules to control nanoparticle spacing.[8,12–16] Understanding of how their structures control properties has been bolstered by electromagnetic simulations of their periodic unit cells. Disordered assemblies of nanoparticles also exhibit collective optical response, but they typically lack the precise and reproducible structural control needed to fully rationalize their spectra. The computational challenge of simulating disordered assemblies has also hampered the understanding and predictive design of their optical properties.[17,18]

Nanocrystal gels are percolated networks of linked colloidal nanocrystals lacking long-range order, which show great promise as tunable and responsive optical materials if these challenges can be overcome.[17,19–23] In contrast to close-packed nanocrystal assemblies,[24,25] nanocrystal gels can incorporate nanocrystals with different compositions and without specific size or shape constraints, enabling the emergence of collective properties from diverse building blocks.[26,27] Discrete, disordered assemblies of nanoparticles, like clusters and strings, have been shown to exhibit collective plasmonic response that varies with their structural attributes,[28–33] yet their spectra could be only qualitatively compared to simulations, owing to structural heterogeneity.[34,35] In our own recent work, we showed that thermoreversible metal-coordination links[36,37] result in reproducible structures and consistent assembly-induced optical changes in single- and multi-component gel networks of ITO nanocrystals, but we lacked a mechanism to systematically tune gel structures and the resulting optical properties.[10,27]

Here, we bring the structure of plasmonic ITO nanocrystal gels under chemical control and show that their infrared optical spectra can be rationally tuned by selecting nanocrystal building blocks and tailoring the molecular structures of the surface ligands that govern the gap distance between neighboring nanocrystals. We find that the redshift in LSPR peak when forming gels from nanocrystal dispersions increases gradually with higher tin doping concentration, larger nanocrystal size, and shorter ligand molecules, parameters that are conveniently adjustable through synthetic tuning of the inorganic core and the surface ligands. We use Brownian dynamics simulations to extract the gap distance from small angle X-ray scattering (SAXS) data,[17,27] leading to the observation of a universal scaling relationship between the relative plasmonic peak shift and scaled gap distance, establishing a "plasmon ruler." The approximate exponential scaling is verified by simulating the optical response of gels with variable gap spacing using a highly efficient mutual polarization method (MPM) we recently developed to compute properties of assemblies containing many thousands of nanoparticles.[17] Analogous to previous analyses of plasmon coupling between pairs of noble metal nanoparticles,[38–40] the plasmon ruler we derive can be used to predict the plasmon peak

frequency in a gel from the characteristics of the nanocrystal and molecular components. To illustrate the utility of these chemical insights, we design and experimentally demonstrate a gelation process with a distinctive optical character, specifically a binary nanocrystal mixture whose spectrum narrows upon assembly, counter to the usual expectation of broadened spectra due to plasmon coupling in disordered structures.

Results and discussion

Preparation of nanocrystal building blocks and gelation.

To analyze the optical behavior of nanocrystal gels under structural and chemical synthetic variation, ITO nanocrystals with varying size and tin doping concentrations (%Sn) were synthesized via a modified slow-injection method[5,41] and subsequently functionalized with length-variable, terpyridine-terminated ligands used for linking ($\mathbf{TL}_n$, n = 2, 4, or 6) (Figure 1 and Table 1). Bright-field scanning transmission electron microscopy (BF-STEM) images show the uniform, quasi-spherical morphology of the ITO nanocrystals regardless of their size and %Sn (Figure 1b and Figures S4 and S5). The monodisperse nanocrystal size was further confirmed by fitting SAXS of nanocrystal dispersions using a spheroid form

Table 1: Characterization of oleate-ITO nanocrystals. Sn doping concentration was found by inductively coupled plasma mass spectrometry (ICP-MS) analysis of digested nanocrystals and the uncertainty in diameter (d_{core}) is based on SAXS fitting.

Sn doping (at.%)	d_{core} (nm)	ω_{LSPR} (cm^{-1})	FWHM (cm^{-1})
3.5	12.1 ± 1.1	4290	1180
4.5	11.9 ± 1.1	4506	1249
5.5	12.6 ± 1.2	4895	1357
7.4	12.2 ± 1.2	5281	1482
8.4	12.4 ± 1.5	5480	1622
5.5	14.4 ± 1.1	5002	1068
5.2	16.4 ± 1.2	5088	1177
5.4	19.5 ± 1.7	5137	989

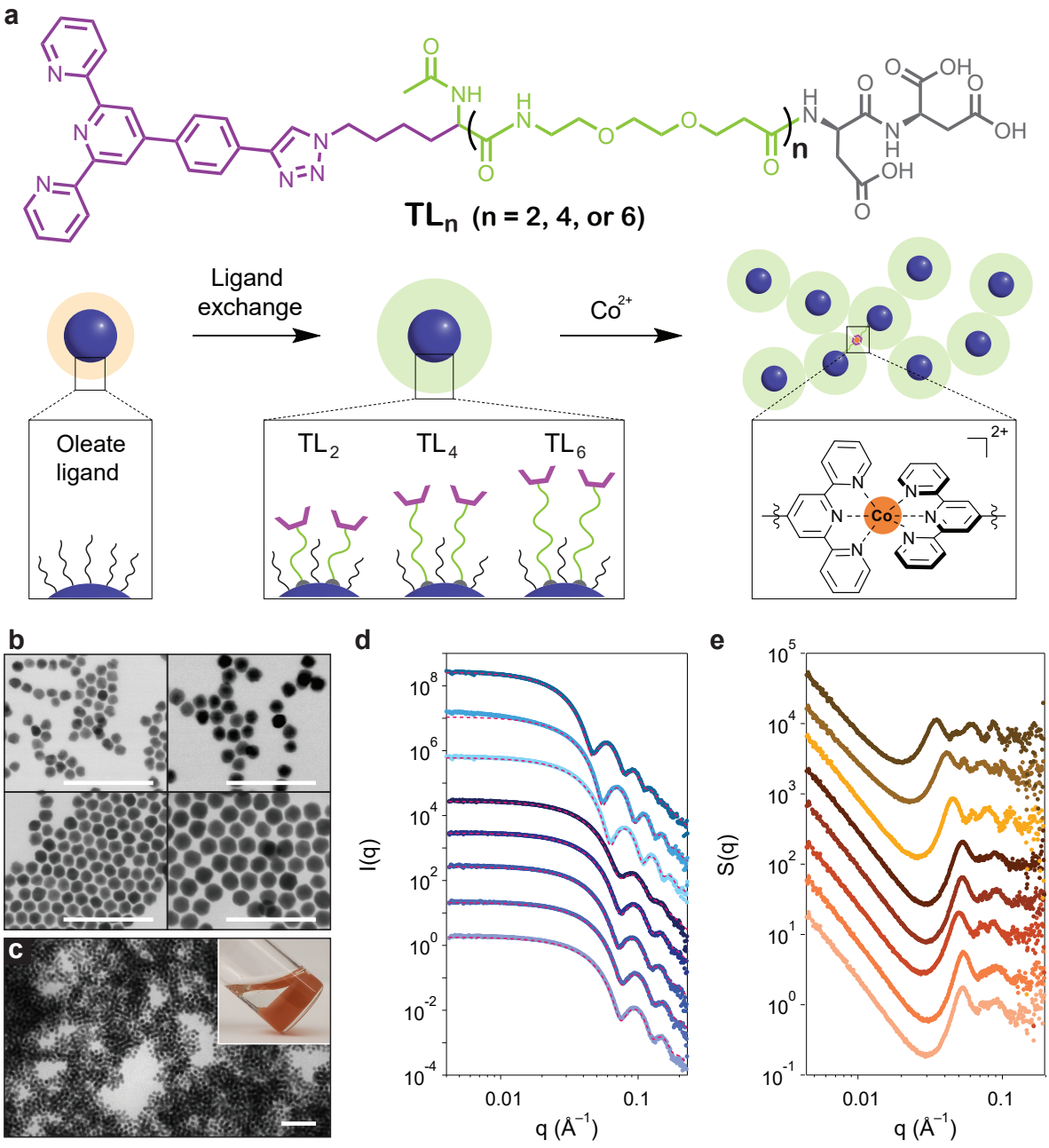

Figure 1: Preparation of TL$_n$-ITO and nanocrystal gelation. **a**, Schematics showing functionalization of oleate-capped ITO nanocrystals (oleate-ITO) with terpyridine-terminated ligands with varying length (**TL**$_n$, n = 2, 4, or 6) and assembly of **TL**-ITO via metal coordination bonding. STEM images of **b**, oleate-ITO with diameters of 12.6, 14.4, 16.4 and 19.5 nm and **c**, a representative gel constituted of **TL**$_2$-ITO with an inset photo. Scale bars, 100 nm. **d**, SAXS patterns (solid dots) with spheroid fits (dashed lines) of oleate-ITO dispersed in hexane and **e**, SAXS structure factors $S(q)$ of corresponding nanocrystal gels assembled from **TL**$_2$-ITO. Both SAXS patterns and $S(q)$ are offset for clarity.

factor, revealing negligible aggregation and a narrow size polydispersity of approximately 10%. (Figure 1d and Table 1). To facilitate thermoreversible nanocrystal gelation, oleate-capped ITO nanocrystals (oleate-ITO) were subjected to direct ligand exchange with **TLs**, consisting of a terpyridine terminal domain, a solubilizing polyethylene oxide-like backbone, and tricarboxylate anchor for binding to the nanocrystal surface (Figure 1a). The ligands were synthesized using established protocols[10,27] with a modification to vary the number of polyethylene oxide units in the ligand backbone, enabling manipulation of its length (Figures S1–S3). The Fourier-transform infrared spectroscopy (FTIR) of **TL**-ITO shows characteristic peaks of **TL** in the fingerprint region, with the absence of the ν(C=O) peak at 1726 cm^{-1} observed in **TL**, indicating that **TL** is attached to the nanocrystal surface via the tricarboxylate domain (Figure S6). Adding cobalt(II) ions to a dispersion of **TL**-ITO in the presence of excess Cl^- establishes an equilibrium between freely dissolved $CoCl_4^{2-}$ and cobalt(II)-(bis)terpyridine ($Co(Tpy)_2$) linkages, leading to gelation (Figure 1c, inset). BF-STEM of a gel shows open, porous networks of linked nanocrystals (Figure 1c). Regardless of size and doping concentration, log-log plots of nanocrystal gel SAXS structure factors $S(q)$ exhibited linear regions at low q with slopes indicating fractal dimensions of 2.0-2.4, implying consistent mesoscale arrangement of nanocrystals (Figure 1e). Higher temperatures favor the dissociation of $Co(Tpy)_2$ links and formation of free $CoCl_4^{2-}$, breaking up the gel and dispersing the nanocrystals. The full thermoreversibility of our gels was indicated by the close resemblance between the infrared response of oleate-ITO dispersed in trichloroethylene (TCE) and $\mathbf{TL}_2$-ITO disassembled from gels in dimethylformamide (DMF) at 100 °C (Figure S7).

Spectral tuning of gels via nanocrystal size and doping.

The synthetically tunable size and doping concentration of ITO nanocrystals impact their optical absorption[4] and we expected that these chemically controllable characteristics could also systematically influence the optical response of gels assembled from these building blocks.

To examine the impact of doping concentration, a series of gels were prepared using $\mathbf{TL}_2$ and nanocrystals with a consistent diameter d_{core} (12.2 ± 0.3 nm) and varying %Sn (ranging from 3.5 to 8.4 Sn at.%) as determined by inductively coupled plasma-mass spectrometry (ICP-

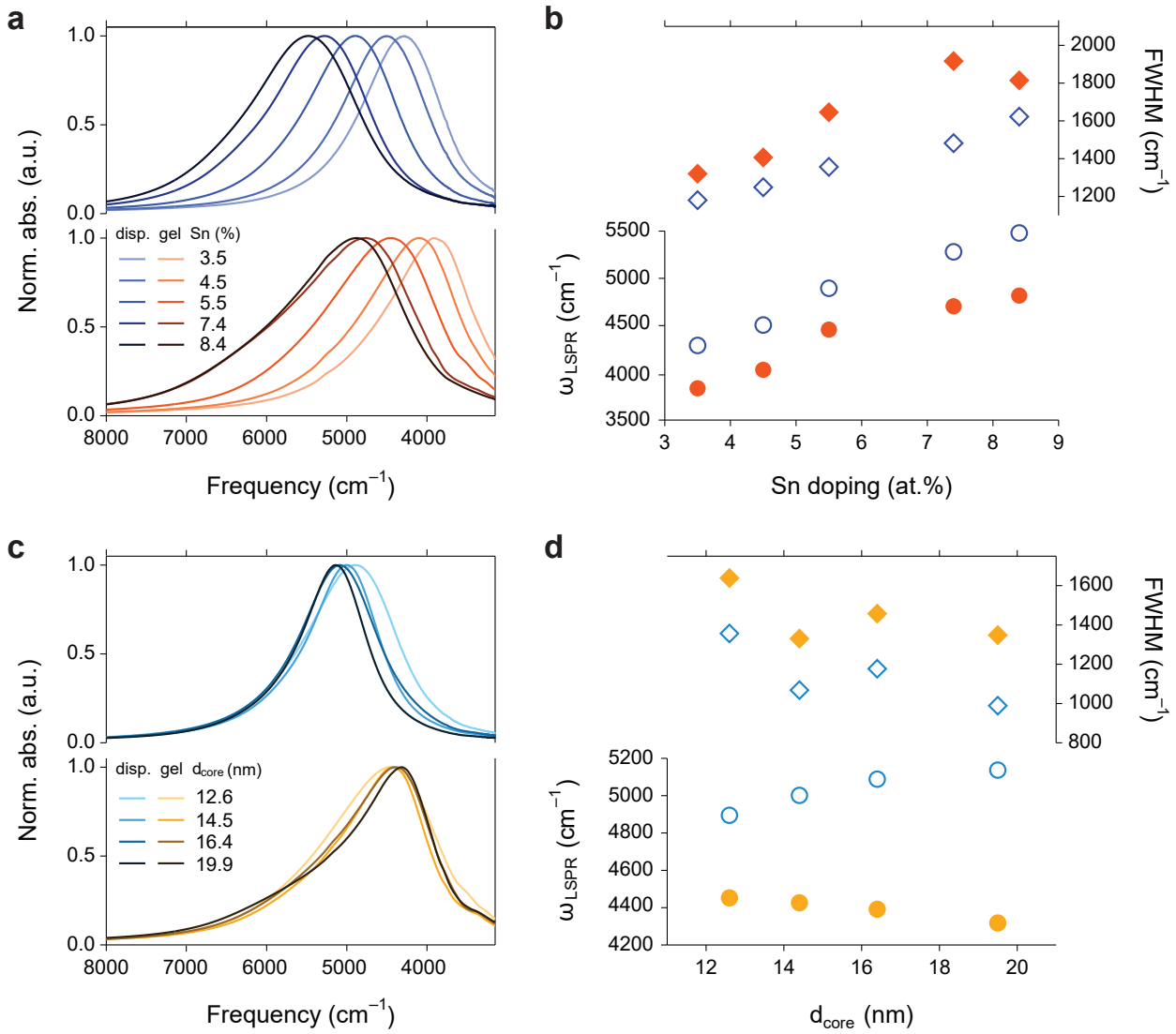

Figure 2: Infrared optical modulation of gels via nanocrystal size and doping. **a**, Infrared absorption of nanocrystals with the same size and different tin doping concentration dispersed in TCE (top) and of their corresponding nanocrystal gels in DMF (bottom). **b**, LSPR peak position (ω_{LSPR}) and full width at half maximum (FWHM) of nanocrystal dispersions and gels composed of nanocrystals with the same size and different %Sn. **c**, Infrared absorption of nanocrystals with the same %Sn and different size dispersed in TCE (top) and of their corresponding nanocrystal gels in DMF (bottom). **d**, ω_{LSPR} and FWHM of nanocrystal dispersions and gels composed of nanocrystals with the same %Sn and different size.

MS). Upon gelation, the infrared absorption spectra of nanocrystals evidently redshifted and broadened regardless of doping concentration, a signature of LSPR coupling between assembled plasmonic building blocks (Figure 2a). Monitoring LSPR peak position (ω_{LSPR}) and full width at half maximum (FWHM) of nanocrystal dispersions and gels allowed for a more quantitative analysis of the doping effect on plasmon coupling (Figure 2b). Overall, the gels displayed the same qualitative trend in the peak features compared to nanocrystal dispersions, characterized by increasing ω_{LSPR} and FWHM with higher %Sn. The differences in the peak features between nanocrystal dispersion and gel ($\Delta\omega_{\mathrm{LSPR}}$ and ΔFWHM), however, became increasingly prominent with higher %Sn due to stronger LSPR coupling.

Similarly, to investigate the size effect on their optical response, a series of gels were prepared using $\mathbf{TL}_2$ and nanocrystals with a consistent doping content (5.4 $\pm$ 0.1 Sn at.%) and varying d_{core}, ranging from 12.6 to 19.5 nm. Nanocrystal dispersions showed mildly increasing ω_{LSPR} and decreasing FWHM with larger d_{core} due to higher electron concentration and decreased electron damping, consistent with previous findings (Figure 2c,d).[4] Similar to the doping concentration effect, $\Delta\omega_{\mathrm{LSPR}}$ and ΔFWHM monotonically increased with larger d_{core}, implying enhanced plasmon coupling. Hence the synthetically controlled size and %Sn of the individual nanocrystals impact the strength of their interactions that governs the emergent properties of the gels systematically and predictably.

Spectral tuning of gels via ligand length.

In addition to the physicochemical variation of inorganic cores, the plasmon coupling in gel assemblies can be further adjusted by manipulating the interparticle spacing through synthetic variations of ligand length. To synthesize the length-variable ligands, the number of repeating units in polyethylene oxide-based ligand backbone was adjusted to 2, 4, and 6 ($\mathbf{TL}_2$, $\mathbf{TL}_4$, and $\mathbf{TL}_6$, respectively). Identical oleate-ITO with 12.6 nm diameter and 5.5 %Sn were separately functionalized with the 3 different-length ligands and assembled into gels under otherwise identical conditions. Although the inorganic cores were of the same

size, the use of longer ligands shifted the position of the primary peak in SAXS $S(q)$ towards lower q, indicating an expansion of the interparticle spacing (Figure 3a). Additionally, the mesoscale organization of nanocrystals transformed into a more compact structure as longer ligands were employed, as evidenced by an increase in the fractal dimension from 2.2 to 2.9. To investigate the effect of ligand length on the gelation process, LSPR absorption spectra of the thermoreversible gels comprising $\mathbf{TL}_n$-ITO (n = 2, 4, and 6) were separately monitored in situ at varying temperatures (Figure 3b,c and Figure S8). At 100 °C, irrespective of the ligand employed, ω_{LSPR} of the gel forming mixture was similar to that of a $\mathbf{TL}_n$-ITO dispersion in the absence of any cobalt(II) linker, indicating that the nanocrystals were effectively dispersed. However, as the temperature decreased, the formation of enthalpically stable $\mathrm{Co(Tpy)_2}$ links becomes increasingly favorable, interconnecting nanocrystals within the gel assemblies and causing a sudden decrease in ω_{LSPR} due to LSPR coupling upon gelation. Despite utilizing the same linking chemistry (i.e., consistent ΔH) and inorganic core, the apparent gelation temperature was noticeably lower when longer ligands were employed. This trend can be attributed to the additional entropic advantage gained by longer ligands when they are not forming links, lowering Gibbs free energy change ($\Delta G = \Delta H$ - $T\Delta S$) for

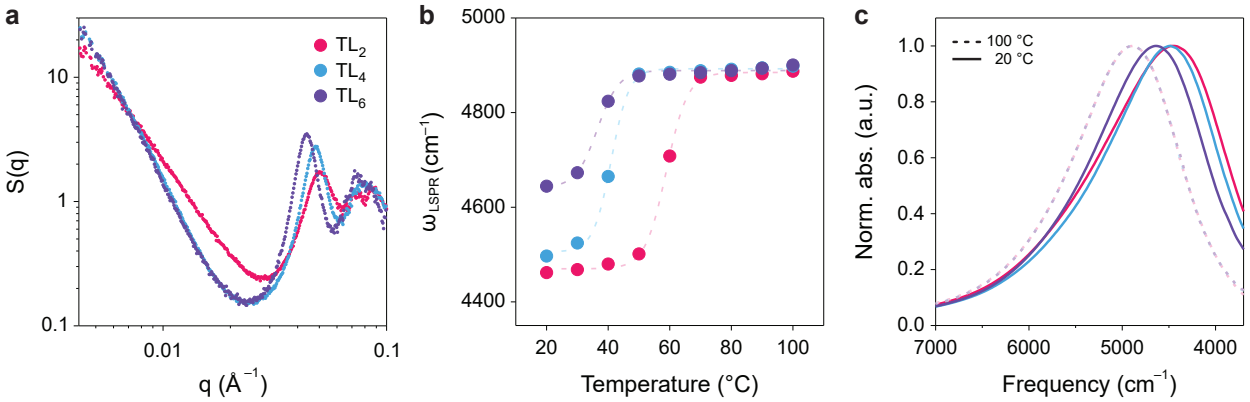

Figure 3: Infrared optical modulation of gels via ligand length. **a**, SAXS $S(q)$ of nanocrystal gels comprising the same nanocrystals functionalized by terpyridine-terminated ligands with varying length ($\mathbf{TL}_n$, n = 2, 4, and 6). **b**, ω_{LSPR} monitored in situ at varying temperatures and **c**, infrared absorption spectra at 30 °C of the thermoreversible $\mathbf{TL}_n$-ITO gel assemblies in DMF.

bond dissociation compared to shorter ligands. Thermodynamic perturbation theory and Langevin dynamics simulations have predicted similar trends in the formation temperatures of polymer-linked patchy colloid networks.[42] The denser mesoscale structure observed in gels with longer ligands, as evidenced by SAXS $S(q)$, may be attributed to the slower cooling rate during gel formation at lower temperatures where these gels form owing to the smaller thermal gradient between the material and ambient, which allows more time for nanocrystal rearrangement to reach a more stable structure. Despite this structural evolution implying higher valence, the infrared absorption spectra of gels with longer ligands exhibited lesser redshift in ω_{LSPR}, suggesting that the shorter interparticle spacing has more dominant impact in plasmon coupling over the denser mesoscale structure (Figure 3c).

Plasmon ruler and design of gels optical response.

The manifold trends in LSPR spectra based on synthetically tunable changes in the nanocrystals and ligands can be rationalized by comparing the scaled plasmon peak shift upon gelation ($\Delta\omega/\omega_{\mathrm{disp}}$) to the scaled interparticle gap distance ($\mathrm{Gap}/d_{\mathrm{core}}$). All the synthesized samples approximately follow a single-exponential decay function where the peak shift diminishes for larger relative spacing, confirming the predominant effect of interparticle spacing on the strength of plasmon coupling in our gels (Figure 4a and Figures S9 and S10). When the normalized peak shift was plotted using the conventional wavelength units ($\Delta\lambda/\lambda_{\mathrm{disp}}$, nm/nm), the decay constant τ was determined to be 0.24 (Figure S10), which is larger than the typical value found in the plasmon ruler equation for dimers consisting of noble metal nanospheres (0.14 to 0.22)[38,43–46] and smaller than that for noble metal superlattices (0.4 to 0.6).[47,48] This intermediate scaling reflects the valence in nanocrystal gels, placing them on a continuum between the two extremes of nanocrystal assemblies. However, we note that the exponential decay length of our metal oxide nanocrystal gels may not be directly comparable to that of metal nanoparticle assemblies, since the presence of a near-surface depletion region in ITO nanocrystals may diminish the coupling strength.[4,49] Meanwhile, the exponential decay be-

havior of plasmon spectral shift was reproduced in simulations of gel extinction using MPM (Figure 4a and Figure S11). Nanocrystal gels were first assembled using Brownian dynamics simulations of particles with strong, short-ranged attractions at fixed thermodynamic volume fraction. MPM simulations at varying gap distances were then performed by fixing the particle centers and varying the radius of the optical cores.[17,27] The thermodynamic volume fraction and nanocrystal dielectric function were chosen to be qualitatively representative of the suite of experimental ITO nanocrystal gels (Figure S12 and Table S1), but the decay length τ does not change significantly if these parameters are varied.

Having established the scaling relationship that describes how the attributes of nanocrystals and ligands systematically control the optical properties of gels, we sought to design distinct processes that use the same nanocrystal building blocks and leverage structural control

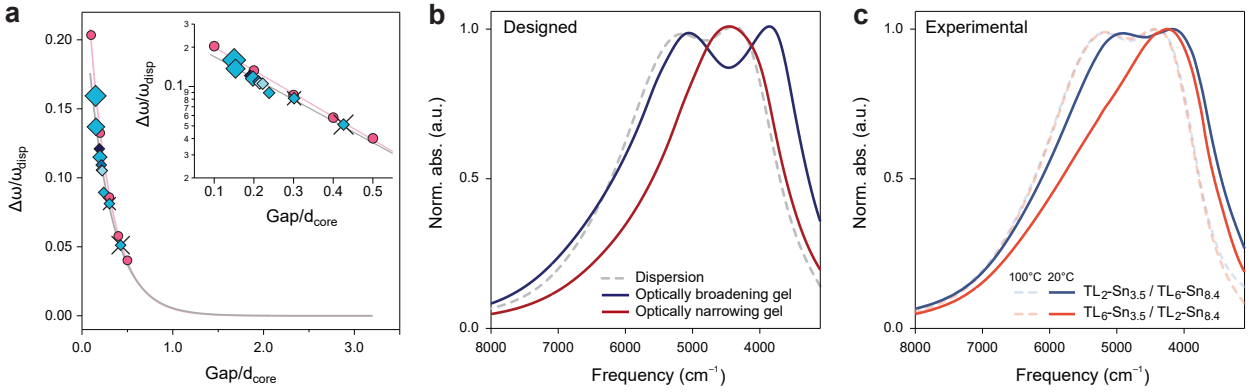

Figure 4: Design and demonstration of gels optical response via plasmon ruler. a, Experimentally measured (blue diamonds) and simulated (red circles) normalized plasmon shift ($\Delta\omega/\omega_{\text{disp}}$, cm^{-1}/cm^{-1}) as a function of normalized gap distance (Gap/d_{core}), with a single-exponential decay fit $y = Ae^{-x/\tau}$ (curves). The inset shows a semi-log plot. Fit parameters were determined to be $A = 0.25 \pm 0.02$ and $\tau = 0.26 \pm 0.02$ for experiment and $A = 0.30 \pm 0.01$ and $\tau = 0.25 \pm 0.01$ for simulations. The size and color of diamond markers indicates the core size and Sn doping concentration (darker color indicates higher %Sn), respectively, of nanocrystal building blocks used. $\mathbf{TL}_4$ and $\mathbf{TL}_6$ are shown as short and long arms of diamond symbols, while $\mathbf{TL}_2$ data points are shown without arms. **b**, Designed infrared response of two thermoreversible nanocrystal assemblies exhibiting identical infrared absorption in the dispersed state (100 °C, dashed) and distinct optical response upon gelation (20 °C, solid). **c**, Experimental optical response of mixed nanocrystals comprising 6:4 (v:v) $\mathbf{TL}_2$-$Sn_{3.5}$:$\mathbf{TL}_6$-$Sn_{8.4}$ (blue) and $\mathbf{TL}_6$-$Sn_{3.5}$:$\mathbf{TL}_2$-$Sn_{8.4}$ (orange) at 100 °C (dashed) and 20 °C (solid). $\mathbf{TL}_n$-Sn_x indicates $\mathbf{TL}_n$-ITO with 12 nm diameter and x at. %Sn.

to deliberately broaden or counterintuitively narrow the spectral linewidth upon gelation. To accomplish this, we considered two-component nanocrystal gels, as we had already observed that single-component gels, regardless of the size and doping concentration of the inorganic core, or the length of the ligands, exhibited optical broadening when compared to their corresponding dispersions. We hypothesized that a narrowing optical spectrum upon gelation can be achieved by maximizing the spectral shift of a high-frequency nanocrystal component and simultaneously minimizing the redshift of a low-frequency component. Guided by the plasmon ruler that can predict the redshift ($\Delta\omega$) for a given nanocrystal based on its resonance peak in dispersion (ω_{disp}) and ligand length compared to nanocrystal size ($\text{Gap}/d_{\text{core}}$), we selected a mixture of functionalized nanocrystals. Nanocrystals with high %Sn (8.4 at.%) were functionalized with short ligands ($\mathbf{TL}_2$), those with low %Sn (3.5 at.%) were functionalized with long ligands ($\mathbf{TL}_6$), and the two were mixed in a 4:6 (v:v) ratio. The mixed nanocrystal dispersion showcased two distinct peaks, resulting from the significant spectral separation of 1190 cm^{-1} between the high- and low-frequency components. From our single component gel experiments, we knew the 8.4 %Sn nanocrystals functionalized with $\mathbf{TL}_2$ exhibited a substantial 663 cm^{-1} shift upon gelation. From the plasmon ruler we derived (Figure 4a), we estimated that the redshift of the 3.5 %Sn nanocrystals with long $\mathbf{TL}_6$ ligands would only be 199 cm^{-1} (see Supporting Information 3.3), suggesting the resonance peak offset between the two components could be reduced to around 700 cm^{-1} in a mixed gel. Using the plasmon ruler-predicted shifts, we calculated a predicted spectrum with a single, narrowed peak for the combined gel (Figure 4b and Figure S13).

Indeed, while the mixed nanocrystal dispersion spectrum taken at 100 °C has two distinct peaks, the mixed gel spectrum observed at 20 °C exhibits a single, sharpened absorption peak (Figure 4c). In stark contrast to the optical broadening typically resulting from plasmon coupling in nanocrystal assemblies, especially disordered assemblies like gels, our mixed gel exhibited a FWHM of 2275 cm^{-1}, which is 160 cm^{-1} less than the FWHM of the corresponding dispersion (2440 cm^{-1}). The narrowing of the absorption spectrum upon gelation is even

more pronounced when considering the full-width at three-quarters maximum (FW3QM), decreasing by 460 cm^{-1}, from 1829 cm^{-1} to 1369 cm^{-1}. Using the same mixture of nanocrystals, but with the ligand lengths reversed between the two components, the plasmon ruler predicts increasing spectral separation of over 1300 cm^{-1} upon gelation resulting in a significantly broadened spectral lineshape (Figure 4b). At 100 °C, the mixture of nanocrystals with switched ligands was spectrally indistinguishable from the mixture described above. However, the gel observed at 20 °C exhibited a broadened infrared response that retained two distinct peaks (Figure 4c). The spectral width of the gel exceeded that of the dispersion, with an increase of 207 cm^{-1} and 88 cm^{-1} in FWHM and FW3QM, respectively. Designing the spectral broadening or narrowing upon gelation is just one example highlighting how understanding the collective behavior of building blocks under chemical and structural control can facilitate the deliberate tuning of their optical response in nanocrystal gel assemblies.

Conclusions

By capitalizing on the modularity of our thermoreversible nanocrystal gel assemblies, we have achieved a highly versatile optical response that can be easily tuned through straightforward synthetic modifications of the inorganic core and the surface ligand. While the redshift of LSPR upon gelation was gradually increased in correlation with larger inorganic core size, higher Sn doping content, and shorter ligand length, the scaled peak shift as a function of scaled gap distance was found to follow a universal relationship with a more gradual decay than for plasmonic nanodimers and more rapid than for close-packed, high-valence superlattices. This predictable dependence of the optical properties on building block characteristics enables rational design of gel spectral response via tuning the molecular structure of the network. As a demonstration, we designed and experimentally realized a gelation process that resulted in a distinctive reduced spectral width compared to the corresponding nanocrystal dispersion, contrary to the typical optical broadening observed in all single-

component nanocrystal gels and other disordered assemblies. Furthermore, the ability to modularly tune the collective plasmonic response in gel assemblies holds great potential for various applications. For instance, it can be utilized to create optical filters with adjustable spectral windows[50] or achieve precise energy matching for non-linear optics.[51] Structurally distinct gels can also be designed to optimize near-field enhanced processes like plasmon-enhanced fluorescence, surface-enhanced Raman scattering (SERS), and surface-enhanced infrared absorption (SEIRA).[35,52–54] We can envision gels whose structure and optical properties respond to other types of stimuli by incorporating linking chemistries sensitive to light, pH change, mechanical strain, or magnetic fields.[32,33,55–57] Beyond plasmonic properties, such assemblies could have diverse collective behaviors including rheological characteristics, superparamagnetism, and Förster resonance energy transfer (FRET) depending on the choice of nanocrystal and molecular components.

Methods

Synthesis of ligands. Terpyridine-terminated ligands ($\mathbf{TL}_n$) were synthesized by modifying established literature methods.[10] The process involved solid-phase peptide synthesis (SPPS) to create ligands with varying repeating units (n = 2, 4, and 6). The ligand was assembled on solid support resin, and an azido lysine was utilized during SPPS to incorporate a terminal azide functional group. Subsequently, the terpyridine-based alkyne moiety was attached to the ligand using copper azide alkyne cycloaddition (CuAAC). After completion, the ligands were released from the resin, purified via high-performance liquid chromatography, and dried for further use.

Synthesis and functionalization of nanocrystals. ITO nanocrystals were synthesized on a Schlenk line through a modification of a slow growth procedure.[5] A precursor solution containing Sn(IV)acetate and In(III)acetate in 10 mL oleic acid was degassed (90 °C, 1 h) and heated (150 °C, 3 h) under flowing nitrogen. The solution was then slowly injected into 13 mL oleyl alcohol at 290 °C under nitrogen flow. Sn doping was controlled by varying Sn(IV)/In(III) molar ratio, while nanocrystal size was adjusted by changing precursor injection volume. After synthesis, nanocrystals were washed five times with ethanol and dispersed in hexane.

The nanocrystals were functionalized through a direct ligand exchange.[41] As-synthesized, oleate-capped nanocrystals were precipitated into a pellet and sonicated in a ligand solution (0.01 M $\mathbf{TL}_n$ in DMF) for 2 h. The functionalized nanocrystals were washed three times with a 3:7 (v:v) EtOH:hexane mixture and then dispersed in pure DMF.

Preparation of samples for spectroscopic measurement. The samples were prepared by adding anhydrous $CoCl_2$ (0.01 M, in DMF) and TBACl (0.5 M, in DMF) to a dispersion of $\mathbf{TL}_n$-ITO (40.0 mg/mL, in DMF). The final volume fraction of nanocrystal was adjusted to 0.001 by adding neat DMF. The final concentration of $CoCl_2$ and TBACl

was fixed at 0.5 mM and 150 mM, respectively. The nanocrystal solution was then heated on a hotplate set at 120 °C until it formed a uniform, free-flowing dispersion. This dispersion was subsequently injected into a temperature-controlled liquid cell for UV-vis-NIR spectroscopy.

Brownian dynamics simulation of nanocrystal gels. We performed BD simulations of $N = 8000$ nanocrystals of thermodynamic hard sphere radius b in a cubic periodic box of volume V at a thermodynamic volume fraction $\eta = 4\pi b^3 N/V = 0.20$ using HOOMD-Blue (v2.9.7).[58] Nanocrystals interacted via hard sphere repulsion for $r < 2b$

$$U^{\mathrm{HS}}(r) = \frac{\gamma^H}{4\Delta t}\big(r-b\big)^2 \tag{1}$$

and the Asakura-Oosawa short-ranged attraction[59] for $2b \leq r \leq 2b + 2\delta$,

$$U_{ij}^{\mathrm{attr}}(r) = -\frac{\varepsilon_{\mathrm{attr}}(b+\delta)^3}{\delta^2(3b/2+\delta)}\left(1 - \frac{3}{4}\frac{r}{b+\delta} + \frac{1}{16}\left(\frac{r}{b+\delta}\right)^3\right) \tag{2}$$

Here, $\gamma_i^H = 6\pi\mu b$ is the Stokes hydrodynamic drag coefficient in a fluid of viscosity μ, $\Delta t = 10^{-4}\tau_D$ is the integration time step, $\tau_D = \gamma^H b^2/k_B T$ is the diffusion time, $\varepsilon_{\mathrm{attr}} = 10k_B T$ is the strength of the attraction at contact $r = 2b$, and $\delta = 0.1b$ is the range of the attractive potential. Note that this form of the hard-sphere repulsion separates two overlapping particles to contact over a single time step and is therefore functionally equivalent to the Heyes-Melrose algorithm for hard spheres.[60] Particles were initialized on a simple cubic lattice and allowed to equilibrate with only hard sphere repulsions for $500\tau_D$. The attractions were then turned on, the suspension evolved for $10000\tau_D$, and assembled configurations were sampled over $1000\tau_D$.

The three-dimensional structure factor $S(\mathbf{q})$ was computed

$$S(\mathbf{q}) = \frac{1}{N} \sum_{ij} e^{i\mathbf{q}\cdot(\mathbf{x}_i - \mathbf{x}_j)} \tag{3}$$

where $\mathbf{x}_i$ is the position of i. We then calculated $S(q)$ by averaging $S(\mathbf{q})$ values whose $q = |\mathbf{q}|$ are within $\Delta q = 2\pi/L$. $S(q)$ is averaged over 100 configurations. The thermodynamic hard sphere sizes were found by comparing the simulated and experimental structure factors of nanocrystal gels and selecting the b that aligned the positions of the primary peak in $S(q)$ (Figure S14). The gap distance is then defined as twice the difference between this thermodynamic hard sphere radius b and the bare nanocrystal core radius a from SAXS measurements of dilute dispersions (Table 1 and Figure S9)

$$\text{Gap} = 2b - 2a \tag{4}$$

Optical simulations using the mutual polarization method. The dielectric function of the nanocrystals $\varepsilon_p(\omega)$ was estimated with a Drude model

$$\varepsilon_p = \varepsilon_\infty - \frac{\varepsilon_0 \omega_p}{\omega^2 + i\gamma\omega} \tag{5}$$

where ω is the frequency, ε_0 is the vacuum permittivity, $\gamma = 0.10\,\omega_p\sqrt{\varepsilon_0/\varepsilon_m}$ is the damping coefficient, $\varepsilon_m = 2.04$ is the permittivity of the DMF background fluid, and $\varepsilon_\infty = 4\varepsilon_0$ is the high-frequency permittivity of ITO.

The optical response of the assembled nanocrystals when irradiated by light with electric field polarization $\mathbf{E}_0$ was computed using MPM,[17] which determines the many-bodied

induced dipoles $\mathbf{p}_i$ of each nanocrystal i by solving the system of equations

$$\mathbf{E}_0 = \sum_j \mathbf{M}_{ij} \cdot \mathbf{p_j}, \qquad \mathbf{M}_{ij} = \begin{cases} \dfrac{1}{4\pi a^3 \varepsilon_m \alpha_i} \mathbf{I} & i = j \\ \dfrac{1}{4\pi \varepsilon_m r^3} \left(\mathbf{I} - 3\hat{\mathbf{r}}\hat{\mathbf{r}}\right) & i \neq j \end{cases} \tag{6}$$

where $\alpha = (\varepsilon_p - \varepsilon_m)/(\varepsilon_p + 2\varepsilon_m)$, $\mathbf{r} = \mathbf{x}_i - \mathbf{x}_j$, $r = |\mathbf{r}|$, $\hat{\mathbf{r}} = \mathbf{r}/r$, and $\mathbf{I}$ is the identity tensor. The j sum in (6) runs over all nanocrystals and their periodic images and details of solving (6) are in Ref. 17. The effective extinction cross-section per volume nanocrystal is then computed

$$\sigma = \sum_i \frac{3\sqrt{\mu_m}\omega}{4\pi a^3 \sqrt{\varepsilon_m} E_0^2} \operatorname{Im}\left[\mathbf{p}_i \cdot \mathbf{E}_0\right] \tag{7}$$

where μ_m is the permeability of the background medium. σ is averaged over three independent field polarizations $\mathbf{E}_0 = E_0 \hat{\mathbf{e}}_i$, $i = x, y, z$.

Associated Content

Supporting Information

Synthetic protocols of ITO nanocrystals and terpyridine-terminated ligands ($\mathbf{TL}_n$), descriptions on instrumentation including Scanning Transmission Electron Microscopy (STEM), UV-Vis-NIR spectroscopy, Small-Angle X-ray Scattering (SAXS), Fourier Transform Infrared Spectroscopy (FTIR), Inductively Coupled Plasma-Mass Spectroscopy (ICP-MS), ligand functionalization procedure, nanocrystal gel preparation, and calculation of expected IR absorption spectra of gels, and supporting figures S1-S14.

Author contributions

J. K. and Z. M. S. contributed equally to this work. J. K. and D. J. M. conceived the idea and designed the research. D. J. M., T. M. T., and E. V. A. guided the research. J. K. and M. N. D. performed synthesis of nanocrystals, material characterization, and UV-vis-NIR

spectroscopy. D. L. C., H. S. N. C., and S. A. V. designed, synthesized, and characterized ligands. Z. M. S. performed BD and MPM simulations. J. K., D. J. M., Z. M. S., D. L. C. and T. M. T. wrote the manuscript with input from all authors.

Notes

The authors declare no competing financial interest.

Acknowledgements

This work was primarily supported by the National Science Foundation through the Center for Dynamics and Control of Materials: an NSF MRSEC under Cooperative Agreement Nos. DMR-1720595 and DMR-2308817. This work was also supported by an Arnold O. Beckman Postdoctoral Fellowship (ZMS) and by the Welch Foundation (Grant Nos. F-1696 and F-1848). EVA acknowledges support from the Welch Regents Chair (F-0046). We acknowledge the Texas Advanced Computing Center (TACC) at The University of Texas at Austin for providing HPC resources.

Data availability

The data that support the findings of this study are available from the corresponding authors upon reasonable request.

References

(1) Liu, X.; Swihart, M. T. Heavily-doped colloidal semiconductor and metal oxide nanocrystals: an emerging new class of plasmonic nanomaterials. *Chem. Soc. Rev.* **2014**, *43*, 3908–3920.

(2) Agrawal, A.; Cho, S. H.; Zandi, O.; Ghosh, S.; Johns, R. W.; Milliron, D. J. Localized surface plasmon resonance in semiconductor nanocrystals. *Chem. Rev.* **2018**, *118*, 3121–3207.

(3) Tandon, B.; Gibbs, S. L.; Zydlewski, B. Z.; Milliron, D. J. Quantitative analysis of plasmonic metal oxide nanocrystal ensembles reveals the influence of dopant selection on intrinsic optoelectronic properties. *Chem. Mater.* **2021**, *33*, 6955–6964.

(4) Staller, C. M.; Gibbs, S. L.; Saez Cabezas, C. A.; Milliron, D. J. Quantitative analysis of extinction coefficients of tin-doped indium oxide nanocrystal ensembles. *Nano Lett.* **2019**, *19*, 8149–8154.

(5) Jansons, A. W.; Hutchison, J. E. Continuous growth of metal oxide nanocrystals: enhanced control of nanocrystal size and radial dopant distribution. *ACS Nano* **2016**, *10*, 6942–6951.

(6) Cho, S. H.; Roccapriore, K. M.; Dass, C. K.; Ghosh, S.; Choi, J.; Noh, J.; Reimnitz, L. C.; Heo, S.; Kim, K.; Xie, K.; Korgel, B. A.; Li, X.; Hendrickson, J. R.; Hachtel, J. A.; Milliron, D. J. Spectrally tunable infrared plasmonic F,Sn:In_2O_3 nanocrystal cubes. *J. Chem. Phys.* **2020**, *152*, 014709.

(7) Ghosh, S. K.; Pal, T. Interparticle coupling effect on the surface plasmon resonance of gold nanoparticles: from theory to applications. *Chem. Rev.* **2007**, *107*, 4797–4862.

(8) Chen, C.-F.; Tzeng, S.-D.; Chen, H.-Y.; Lin, K.-J.; Gwo, S. Tunable plasmonic response

from alkanethiolate-stabilized gold nanoparticle superlattices: evidence of near-field coupling. *J. Am. Chem. Soc.* **2008**, *130*, 824–826.

(9) Klinkova, A.; Choueiri, R. M.; Kumacheva, E. Self-assembled plasmonic nanostructures. *Chem. Soc. Rev.* **2014**, *43*, 3976–3991.

(10) Kang, J.; Valenzuela, S. A.; Lin, E. Y.; Dominguez, M. N.; Sherman, Z. M.; Truskett, T. M.; Anslyn, E. V.; Milliron, D. J. Colorimetric quantification of linking in thermoreversible nanocrystal gel assemblies. *Sci. Adv.* **2022**, *8*, eabm7364.

(11) Olafsson, A.; Khorasani, S.; Busche, J. A.; Araujo, J. J.; Idrobo, J. C.; Gamelin, D. R.; Masiello, D. J.; Camden, J. P. Imaging infrared plasmon hybridization in doped semiconductor nanocrystal dimers. *J. Phys. Chem. Lett.* **2021**, *12*, 10270–10276.

(12) Zhang, Y.; Lu, F.; Yager, K. G.; Van Der Lelie, D.; Gang, O. A general strategy for the DNA-mediated self-assembly of functional nanoparticles into heterogeneous systems. *Nat. Nanotechnol.* **2013**, *8*, 865–872.

(13) Wang, Y.; Yang, Z.; Wei, J. Surface plasmon resonance properties of silver nanocrystal superlattices spaced by polystyrene ligands. *J. Phys. Chem. C* **2022**, *126*, 4948–4958.

(14) Schulz, F.; Pavelka, O.; Lehmkühler, F.; Westermeier, F.; Okamura, Y.; Mueller, N. S.; Reich, S.; Lange, H. Structural order in plasmonic superlattices. *Nat. Commun.* **2020**, *11*, 3821.

(15) Lu, B.; Vegso, K.; Micky, S.; Ritz, C.; Bodik, M.; Fedoryshyn, Y. M.; Siffalovic, P.; Stemmer, A. Tunable subnanometer gaps in self-assembled monolayer gold nanoparticle superlattices enabling strong plasmonic field confinement. *ACS Nano* **2023**, *17*, 12774–12787.

(16) Ross, M. B.; Ku, J. C.; Vaccarezza, V. M.; Schatz, G. C.; Mirkin, C. A. Nanoscale

form dictates mesoscale function in plasmonic DNA–nanoparticle superlattices. *Nat. Nanotechnol.* **2015**, *10*, 453–458.

(17) Sherman, Z. M.; Kim, K.; Kang, J.; Roman, B. J.; Crory, H. S.; Conrad, D. L.; Valenzuela, S. A.; Lin, E.; Dominguez, M. N.; Gibbs, S. L.; Anslyn, E. V.; Milliron, D. J.; Truskett, T. M. Plasmonic response of complex nanoparticle assemblies. *Nano Lett.* **2023**, *23*, 3030–3037.

(18) Park, S. Y.; Lee, J.-S.; Georganopoulou, D.; Mirkin, C. A.; Schatz, G. C. Structures of DNA-linked nanoparticle aggregates. *J. Phys. Chem. B* **2006**, *110*, 12673–12681.

(19) Gaponik, N.; Herrmann, A.-K.; Eychmüller, A. Colloidal nanocrystal-based gels and aerogels: material aspects and application perspectives. *J. Phys. Chem. Lett.* **2012**, *3*, 8–17.

(20) Rusch, P.; Zámbó, D.; Bigall, N. C. Control over structure and properties in nanocrystal aerogels at the nano-, micro-, and macroscale. *Acc. Chem. Res.* **2020**, *53*, 2414–2424.

(21) Sherman, Z. M.; Green, A. M.; Howard, M. P.; Anslyn, E. V.; Truskett, T. M.; Milliron, D. J. Colloidal nanocrystal gels from thermodynamic principles. *Acc. Chem. Res.* **2021**, *54*, 798–807.

(22) Singh, M.; Sherman, Z. M.; Milliron, D. J.; Truskett, T. M. Linker-templated structure tuning of optical response in plasmonic nanoparticle gels. *J. Phys. Chem. C* **2022**, *126*, 16885–16893.

(23) Arachchige, I. U.; Brock, S. L. Sol–gel methods for the assembly of metal chalcogenide quantum dots. *Acc. Chem. Res.* **2007**, *40*, 801–809.

(24) Cargnello, M.; Johnston-Peck, A. C.; Diroll, B. T.; Wong, E.; Datta, B.; Damodhar, D.; Doan-Nguyen, V. V.; Herzing, A. A.; Kagan, C. R.; Murray, C. B. Substitutional doping in nanocrystal superlattices. *Nature* **2015**, *524*, 450–453.

(25) Shevchenko, E. V.; Talapin, D. V.; Kotov, N. A.; O'Brien, S.; Murray, C. B. Structural diversity in binary nanoparticle superlattices. *Nature* **2006**, *439*, 55–59.

(26) Freytag, A.; Günnemann, C.; Naskar, S.; Hamid, S.; Lübkemann, F.; Bahnemann, D.; Bigall, N. C. Tailoring composition and material distribution in multicomponent cryoaerogels for application in photocatalysis. *ACS Appl. Nano Mater.* **2018**, *1*, 6123–6130.

(27) Kang, J.; Sherman, Z. M.; Crory, H. S.; Conrad, D. L.; Berry, M. W.; Roman, B. J.; Anslyn, E. V.; Truskett, T. M.; Milliron, D. J. Modular mixing in plasmonic metal oxide nanocrystal gels with thermoreversible links. *J. Chem. Phys.* **2023**, *158*, 024903.

(28) Nie, Z.; Fava, D.; Rubinstein, M.; Kumacheva, E. "Supramolecular" assembly of gold nanorods end-terminated with polymer "pom-poms": effect of pom-pom structure on the association modes. *J. Am. Chem. Soc.* **2008**, *130*, 3683–3689.

(29) Zhang, H.; Wang, D. Controlling the growth of charged-nanoparticle chains through interparticle electrostatic repulsion. *Angew. Chem. Int. Ed.* **2008**, *120*, 4048–4051.

(30) Klinkova, A.; Thérien-Aubin, H.; Choueiri, R. M.; Rubinstein, M.; Kumacheva, E. Colloidal analogs of molecular chain stoppers. *Proc. Natl. Acad. Sci. U. S. A.* **2013**, *110*, 18775–18779.

(31) Nie, Z.; Fava, D.; Kumacheva, E.; Zou, S.; Walker, G. C.; Rubinstein, M. Self-assembly of metal–polymer analogues of amphiphilic triblock copolymers. *Nat. Mater.* **2007**, *6*, 609–614.

(32) Moaseri, E.; Bollinger, J. A.; Changalvaie, B.; Johnson, L.; Schroer, J.; Johnston, K. P.; Truskett, T. M. Reversible self-assembly of glutathione-coated gold nanoparticle clusters via pH-tunable interactions. *Langmuir* **2017**, *33*, 12244–12253.

(33) Liu, L.; Gao, Z.; Jiang, B.; Bai, Y.; Wang, W.; Yin, Y. Reversible assembly and dynamic plasmonic tuning of Ag nanoparticles enabled by limited ligand protection. *Nano Lett.* **2018**, *18*, 5312–5318.

(34) Gudjonson, H.; Kats, M. A.; Liu, K.; Nie, Z.; Kumacheva, E.; Capasso, F. Accounting for inhomogeneous broadening in nano-optics by electromagnetic modeling based on Monte Carlo methods. *Proc. Natl. Acad. Sci. U. S. A.* **2014**, *111*, E639–E644.

(35) Solís, D. M.; Taboada, J. M.; Obelleiro, F.; Liz-Marzán, L. M.; García de Abajo, F. J. Toward ultimate nanoplasmonics modeling. *ACS Nano* **2014**, *8*, 7559–7570.

(36) Schubert, U. S.; Eschbaumer, C. Macromolecules containing bipyridine and terpyridine metal complexes: towards metallosupramolecular polymers. *Angew. Chem. Int. Ed.* **2002**, *41*, 2892–2926.

(37) Winter, A.; Hager, M. D.; Newkome, G. R.; Schubert, U. S. The marriage of terpyridines and inorganic nanoparticles: synthetic aspects, characterization techniques, and potential applications. *Adv. Mater.* **2011**, *23*, 5728–5748.

(38) Jain, P. K.; Huang, W.; El-Sayed, M. A. On the universal scaling behavior of the distance decay of plasmon coupling in metal nanoparticle pairs: a plasmon ruler equation. *Nano Lett.* **2007**, *7*, 2080–2088.

(39) Su, K.-H.; Wei, Q.-H.; Zhang, X.; Mock, J.; Smith, D. R.; Schultz, S. Interparticle coupling effects on plasmon resonances of nanogold particles. *Nano Lett.* **2003**, *3*, 1087–1090.

(40) Liu, N.; Hentschel, M.; Weiss, T.; Alivisatos, A. P.; Giessen, H. Three-dimensional plasmon rulers. *Science* **2011**, *332*, 1407–1410.

(41) Dominguez, M. N.; Howard, M. P.; Maier, J. M.; Valenzuela, S.; Sherman, Z. M.; Reimnitz, L. C.; Kang, J.; Cho, S. H.; Gibbs, S. L.; Menta, A. K.; Zhuang, D. L.;

van der Stok, A.; Kline, S. J.; Anslyn, E. V.; Truskett, T. M.; Milliron, D. J. Assembly of linked nanocrystal colloids by reversible covalent bonds. *Chem. Mater.* **2020**, *32*, 10235–10245.

(42) Howard, M. P.; Jadrich, R. B.; Lindquist, B. A.; Khabaz, F.; Bonnecaze, R. T.; Milliron, D. J.; Truskett, T. M. Structure and phase behavior of polymer-linked colloidal gels. *J. Chem. Phys.* **2019**, *151*.

(43) Tabor, C.; Murali, R.; Mahmoud, M.; El-Sayed, M. A. On the use of plasmonic nanoparticle pairs as a plasmon ruler: the dependence of the near-field dipole plasmon coupling on nanoparticle size and shape. *J. Phys. Chem. A* **2009**, *113*, 1946–1953.

(44) Maye, M. M.; Nykypanchuk, D.; Cuisinier, M.; Van Der Lelie, D.; Gang, O. Stepwise surface encoding for high-throughput assembly of nanoclusters. *Nat. Mater.* **2009**, *8*, 388–391.

(45) Kadkhodazadeh, S.; de Lasson, J. R.; Beleggia, M.; Kneipp, H.; Wagner, J. B.; Kneipp, K. Scaling of the surface plasmon resonance in gold and silver dimers probed by EELS. *J. Phys. Chem. C* **2014**, *118*, 5478–5485.

(46) Dolinnyi, A. I. Nanometric rulers based on plasmon coupling in pairs of gold nanoparticles. *J. Phys. Chem. C* **2015**, *119*, 4990–5001.

(47) Ben, X.; Park, H. S. Size dependence of the plasmon ruler equation for two-dimensional metal nanosphere arrays. *J. Phys. Chem. C* **2011**, *115*, 15915–15926.

(48) Yockell-Lelièvre, H.; Gingras, D.; Vallée, R.; Ritcey, A. M. Coupling of localized surface plasmon resonance in self-organized polystyrene-capped gold nanoparticle films. *J. Phys. Chem. C* **2009**, *113*, 21293–21302.

(49) Tandon, B.; Agrawal, A.; Heo, S.; Milliron, D. J. Competition between depletion effects

and coupling in the plasmon modulation of doped metal oxide nanocrystals. *Nano Lett.* **2019**, *19*, 2012–2019.

(50) Yang, J.; Kramer, N. J.; Schramke, K. S.; Wheeler, L. M.; Besteiro, L. V.; Hogan Jr, C. J.; Govorov, A. O.; Kortshagen, U. R. Broadband absorbing exciton–plasmon metafluids with narrow transparency windows. *Nano Lett.* **2016**, *16*, 1472–1477.

(51) Kauranen, M.; Zayats, A. V. Nonlinear plasmonics. *Nat. Photonics* **2012**, *6*, 737–748.

(52) Klinkova, A.; Thérien-Aubin, H.; Ahmed, A.; Nykypanchuk, D.; Choueiri, R. M.; Gagnon, B.; Muntyanu, A.; Gang, O.; Walker, G. C.; Kumacheva, E. Structural and optical properties of self-assembled chains of plasmonic nanocubes. *Nano Lett.* **2014**, *14*, 6314–6321.

(53) Wagner, M.; Seifert, A.; Liz-Marzán, L. M. Towards multi-molecular surface-enhanced infrared absorption using metal plasmonics. *Nanoscale Horiz.* **2022**, *7*, 1259–1278.

(54) Lee, A.; Andrade, G. F.; Ahmed, A.; Souza, M. L.; Coombs, N.; Tumarkin, E.; Liu, K.; Gordon, R.; Brolo, A. G.; Kumacheva, E. Probing dynamic generation of hot-spots in self-assembled chains of gold nanorods by surface-enhanced Raman scattering. *J. Am. Chem. Soc.* **2011**, *133*, 7563–7570.

(55) Şenel, Z.; İçöz, K.; Erdem, T. Tuning optical properties of self-assembled nanoparticle network with external optical excitation. *J. Appl. Phys.* **2021**, *129*, 153106.

(56) Han, X.; Liu, Y.; Yin, Y. Colorimetric stress memory sensor based on disassembly of gold nanoparticle chains. *Nano Lett.* **2014**, *14*, 2466–2470.

(57) Li, J.; Lu, X.; Zhang, Y.; Cheng, F.; Li, Y.; Wen, X.; Yang, S. Transmittance tunable smart window based on magnetically responsive 1D nanochains. *ACS Appl. Mater. Interfaces* **2020**, *12*, 31637–31644.

(58) Anderson, J. A.; Glaser, J.; Glotzer, S. C. HOOMD-blue: a python package for high-performance molecular dynamics and hard particle Monte Carlo simulations. *Comput. Mater. Sci.* **2020**, *173*, 109363.

(59) Asakura, S.; Oosawa, F. On interaction between two bodies immersed in a solution of macromolecules. *J. Chem. Phys.* **1954**, *22*, 1255–1256.

(60) Heyes, D. M.; Melrose, J. R. Brownian dynamics simulations of model hard-sphere suspensions. *J. Non-Newton. Fluid Mech.* **1993**, *46*, 1–28.

Graphical abstract